Aalborg Universitet

AALBORG UNIVERSITY
DENMARK

Frequency domain scanning acoustic microscopy for power electronics

Physics-based feature identification and selectivity

Uhrenfeldt, Christian; Munk-Nielsen, Stig; Beczkowski, Szymon

Frequency domain scanning acoustic microscopy for power electronics: physics-based feature identification and selectivity.

C. Uhrenfeldt[a,*], S. Munk-Nielsen[a], S. Bęczkowski[a]

[a]*Department of Energy Technology, Aalborg University, Pontoppidanstraede 111, 9220 Aalborg, Denmark*

Abstract

In the evaluation of power electronic components non-destructive test methods (NDT) such as scanning acoustic microscopy (SAM) are valuable tools in packaging and failure analysis. As power modules become more compact and power devices thinner, echo overlap and interference can hamper the imaging capability and analysis of the conventional SAM time domain-based imaging techniques. Frequency domain analysis offers increased resolution and contrast but the interpretation and feature identification of waveforms is less obvious and interpretation guidelines have received little attention. In this paper a physics-based analysis of the frequency domain response is presented in a power module case study. The analysis is used to demonstrate physics-based feature selective contrast in such systems and offers guidelines for feature prediction. The approach is verified on full scan datasets from acoustic scans of a hybrid multilayer stack. Distinct features in the echo frequency domain are identified as resonances associated with multiple internal reflections in the layer structure. Where such features may hamper analysis in the conventional approach these can, if properly assigned, be exploited to yield selective and improved contrasts and allow accurate structural and material analysis.

Keywords: Scanning acoustic microscopy, frequency domain, power modules, non destructive evaluation

1. Introduction

Power electronic packaging involves several possible metal joint formations such as soldering, ultrasonic bonding and sintering. The quality of these joints is key since they strongly affect the thermal performance of power devices. Void filled or degraded solder or sinter joints may lead to overheating which in turn may lead to device failure.

A popular, non-destructive method, used to assess the quality of such joints, is scanning acoustic microscopy (SAM). It enables inspection of finished products without tedious sample preparation. It can be employed in lifetime testing, and is easily applied in packaging process development as a feedback tool to inspect for voids, cracking and delamination [1][2].

In commercial scanning acoustic microscopes, targeted for electronics inspection, a transducer emits an acoustic pulse that is focused on the surface or subsurface features of the device. For power electronics applications, transducers use frequencies approximately in the 15–200 MHz range. The specific frequency is a compromise between sufficient acoustic material penetration depth and acceptable resolution. The transducer is rastered over the device and time responses of reflected or transmitted echoes (A-scans) are recorded at each scanning point. In time domain (TD) analysis, contrast images (C-scans) can be obtained by mapping amplitude values within selected time sub-intervals (time gating) at individual pixels and displaying the results as a contrast image [3].

In time domain SAM analysis, on samples with thick layers, the echoes from subsequent interfaces are clearly separated in time which offers an intuitive understanding of the layered structure. However, in more

---

compact and densely packed assemblies, successive echoes may overlap and interfere, which hampers the echo assignment and detection. To that end frequency domain (FD) analysis has been shown to yield improved resolution and contrast in compact electronics [2][4][5][6]. Despite of this, physical analysis and interpretation of frequency domain SAM methods has received little attention (an exception being the detailed study on thin surface films and delamination in [7]). Improving the interpretation guidelines for frequency domain analysis for SAM in power electronics would make the method more accessible for non-specialist operators and help unfold its potential.

In this paper a physics-based analysis of the frequency domain response is presented in a power module case study. The analysis is used to demonstrate physics-based feature selective contrast in such systems. The link between time domain and frequency domain is analyzed, and quantitative comparison between experiments and model predictions is presented. From the analysis rules of thumb for mode estimation and interpretation are given and examples of thickness measurements and material parameter extraction are demonstrated.

2. Experimental case study

As a case study a power module prototype consisting of a 0.5 mm thick bare SiC power diode die, a Cu–AlN–Cu (0.3–0.63–0.3 mm type) direct bonded copper (DBC) substrate and an AlSiC baseplate was used. The layered stack was soldered together using SAC305 leadfree solder alloy. The assembly was repeatedly subjected to a soldering cycle leading to excessive die and DBC void formation making it a suitable test structure for further SAM investigation.

3D data SAM scans were performed using a KSI V8 scanning acoustic microscope from IP Holding with a 25 MHz transducer with ≈ 22 mm focal length and diameter of ≈ 6.5 mm. The full dataset (i.e. A-scans recorded for each pixel) was stored as a data matrix which was imported into MATLAB for further processing using time domain as well as frequency domain methods.

3. Time domain analysis method

From the stored SAM data matrix C-scan greyscale images can be created post-measurement by mapping amplitude values within selected time gating in the A-scans at each raster point (pixel) into greyscale values. Since the propagation of the sound pulse down through the material takes time, sound reflections from deeper lying subsurface features occur at delayed time instances in the A–scans relative to the echos from the surface. By using time gating on echos delayed relative to the surface echo C-scan images of subsurface images can be obtained and depth of the features may be analyzed from the measured time delay and the sound velocity of the intermediate material. Time domain C-scan images, shown in fig. 1, were created for two cases of time gating $t_{g(A-A)}$ and $t_{g(B-B)}$ (detailed in fig. 2) that were specifically chosen to highlight the subsurface solder voids beneath the die and the deeper lying DBC-void features, respectively. In the shown C-scan time domain (TD) images the color scale was inverted to enable a better comparison with frequency based imaging described below and to improve legibility of image detail. As a result voids are seen as black spots on a bright background in the time domain images in fig. 1 (left). Upon inspection of time domain B–B section, targeted for deeper lying features, it can be seen that the die-solder voids are superimposed on DCB voids, contrary to the expectation. The reason is observed by comparing the A-scans shown in fig. 2 which were obtained at locations ❶ and ❷ defined in the schematic in fig. 1 (right) and indicated by red cross-hairs in the images in fig. 1 (left). At location ❶ the A-scan reveals a surface echo and a separated delayed echo from a feature lying deeper in the module structure. At location ❷ (above a die void) an anomalous ringing like echo extends in time from the surface echo and overlaps both $t_{g(A-A)}$ and $t_{g(B-B)}$. From an analysis perspective the overlapping of these features can be misleading and a decoupling possibility would be preferred.
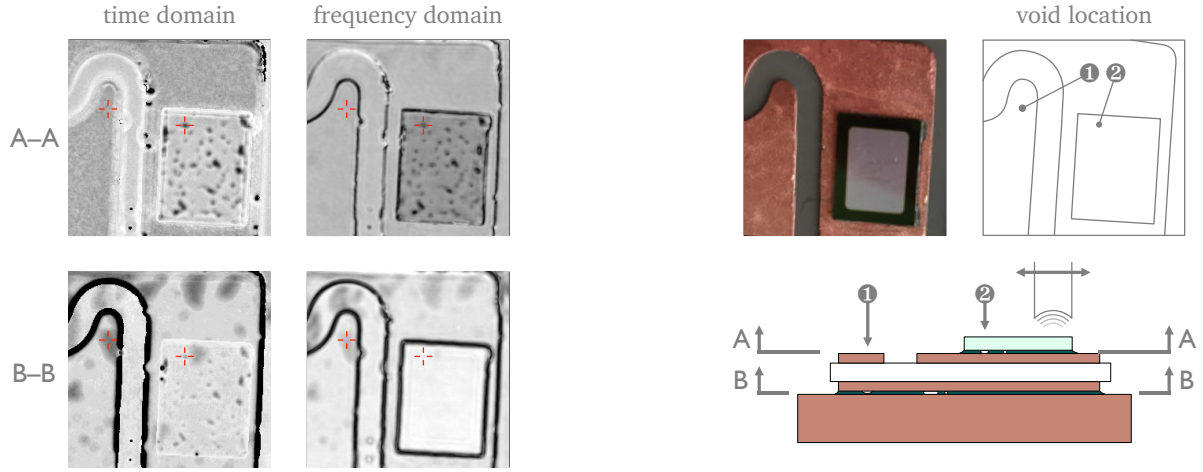
Figure 1: Time domain (TD) and frequency domain (FD) analysis of a power module stack. The color scale was inverted in the TD images (left) to match the appearance in the FD images (middle) and improve legibility. SAM gating set to analyze chip solder (A–A) and DBC solder (B–B). The TD scan of the DBC solder shows ghost images of the chip solder voids. FD image of the same interface is devoid of this problem. ❶ and ❷ indicate A-scan positions used for gating selection. Both positions above solder voids.

4. Frequency domain analysis method

The frequency domain method relies on Fourier analysis of selected time sub-segments of the individual pixel A-scans. First at each pixel the surface reflection position was identified by A-scan threshold triggering. Next, in each A-scan the time region of interest (ROI) to be analyzed is identified relative to the surface trigger. Examples of such selected sub time spans are shown in fig. 2. If very short time spans are used for the subsequent Fourier analysis there is a risk that the time window used crops part of the echo which will introduce effects of the window-function into the spectrum. For this reason subtimespans used here were selected to ensure that the main sampled echo signals were not cropped within the time windows. Subsequently a fast Fourier transform (FFT) was applied to the selected time ROI in MATLAB and the frequency power spectrum was derived for each pixel, examples of which can be seen in fig. 2 (right). By using amplitude values within a narrow sub-frequency interval in the FFT spectra as a basis for pixel-by-pixel contrast generation, frequency-based image contrast can be obtained. From a physical perspective, this can be interpreted as filtering out lower-frequency parts of the echo pulse and the data analysis can be linked to physical analysis of the investigated device or structure.
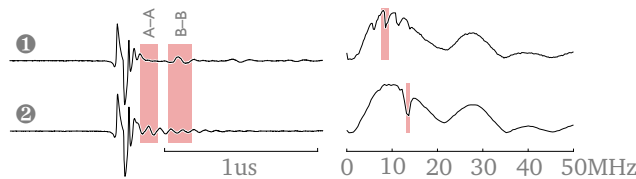
Figure 2: Time domain signals with gating used to target chip and DBC voids $t_{g(A-A)}$ and $t_{g(B-B)}$ (left) and their corresponding FFT spectra with $f_{g(A-A)}$ and $f_{g(B-B)}$ gatings matching specific resonances within the structure (right).

To highlight the selective contrast ability example scans, using both time domain and frequency domain methods are shown in fig. 1. Both methods were used to analyze voids between the chip and the DBC (die voids A–A section in fig. 1), and between DBC and baseplate (DBC voids B–B section in fig. 1) and the same 3D SAM scan data was used. The chip solder voids are clearly visible in both methods, and the time domain approach appears adequate. However when analyzing the DBC solder layer it can be seen that while the

3

time domain images showed chip solder voids superimposed on the DBC solder void image, the frequency domain image enables a separate visualization of the DBC voids. Thus the frequency domain methods enables separation of the void types and bypasses the observed drawback of the time domain method.

This result was obtained by careful selection of the two frequency gating spans $f_{g(A–A)}$ and $f_{g(B–B)}$, shown in fig. 2, that were used to derive the FD contrast images. By comparing the FFT frequency power spectrum and the frequency gating employed it can be seen that the locations ❶ and ❷ on the module show very dissimilar FFT power spectra. At the die-void location the frequency spectrum shows a broadband profile of the transducer echo spectrum modulated by a very distinct dip at a single frequency which was targeted for $f_{g(A–A)}$. At location ❶ the frequency spectrum also shows a broadband spectrum but with a much different modulation which has multiple lower frequency components one of which was targeted for the $f_{g(B–B)}$ image. Since the distinct dips yield a lower signal value than the broadband spectrum, the targeted voids appear dark on a bright background similarly to the color-inverted TD images in fig. 1.
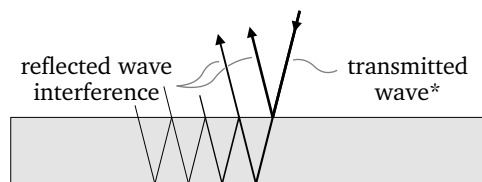

Figure 3: Wave reflections from a single slab of SiC material immersed in water (water above and below the slab is not shown). *Note:* incident wave is normal to the slab. Shown at an angle here for clarity.

5. Theory of operation

To explain the appearance of both time and frequency domain spectra we will first consider the simpler case of multiple reflections in a single layer of SiC (see fig. 3) immersed in water at normal incidence and later expand the analysis to multi-layered structures.

The normal incidence time domain reflected echo signals $s_r(t)$ of a normal incident Gaussian sound pulse A(t) was calculated for normal incidence using the following expression where subsequent delayed reflections are tracked and summed as follows:

$$s_r(t) = \mathrm{Re}\Big\{ r_{12}a(t) + \sum_{n=0}^{\infty} t_{12}r_{23}t_{21}(r_{23}r_{21})^n a(t_n) \Big\}. \tag{1}$$
$$t_n = t - 2\tau_2(n+1)$$

where $a(t)$ is a Gaussian simplified transducer signal which has a maximum at $t = 0$ which for convenience is set at the first surface echo occurrence. The coefficients $r_{ij} = (z_j-z_i)/(z_i+z_j)$ and $t_{ij} = 2z_j\rho_i/(\rho_j(z_i+z_j))$ are the amplitude reflection and transmission coefficient across the interface between layer i and j, $Z_i = \rho_i v_i$ is the acoustic impedance of the i-th layer obtained from data for the material density ρ_i and acoustic longitudinal speed v_i. $\tau_i = d_i/v_i$ is the transit time for the middle layer such that $2\tau_i$ is the delay between successive reflections [8]. For the example with a single slab of SiC material immersed in water, layers 1 and 3 in eq. (1) correspond to the incident and exit medium which both are water in the case here, while layer 2 is the SiC slab which sustains the internal reflections.

The link of eq. (1) to the frequency domain is established by performing the analytic Fourier transform of eq. (1). To that end the Fourier property that the Fourier transform of a time-displaced function $f(t-\tau_i)$ is $e^{i2\pi f\tau_i}F(f)$ is convenient ($F(f)$ is the Fourier transform of the nondisplaced function $f(t)$). With this result the Fourier transform $S(f)$ of $s_r(t)$ becomes:

$$S_r(f) = r_{12}A(f) + t_{12}r_{23}t_{21}e^{i2\phi_2} \sum_{n=0}^{\infty} (r_{23}r_{21}e^{i2\phi_2})^n A(f)$$

$$= \left(r_{12} + \frac{t_{12}r_{23}t_{21}e^{i2\phi_2}}{1 - r_{23}r_{21}e^{i2\phi_2}} \right) A(f)$$

$$= \frac{r_{12} + r_{23}e^{i2\phi}}{1 + r_{12}r_{23}e^{i2\phi}} A(f) = r_{\text{eff}}A(f) \tag{2}$$

$$\phi_i = 2\pi f d_i / v_i = 2\pi f \tau_i = 2\pi d_i / \lambda_i \tag{3}$$

where the property $\sum_{n=0}^{\infty} x^n = 1/(1-x)$ for $|x| < 1$ was used. The term ϕ_2 accounts for the phase change associated with the sound transit across each layer and depends on frequency as well as sound velocity or combined the acoustic wavelength λ_2. Attenuation effects may be incorporated by introducing a properly chosen imaginary part to ϕ_2 [7], but since applicable attenuation data are scarce this was not included.

The time domain $s_r(t)$ echoes using eq. (1) and the corresponding FFT were calculated for the structure shown in fig. 3 for two different thickness of the SiC layer and the result is shown in fig. 4.
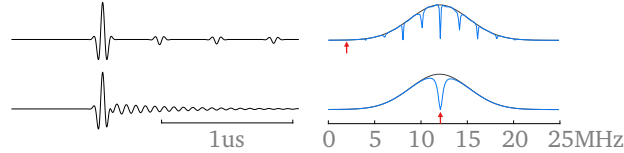

Figure 4:   Theoretical echoes of 3 mm and 0.5 mm SiC slabs (top and bottom, respectively).

At the large thickness of 3 mm the transit time back and forth within the slab is larger than the pulse width and the multiple echoes are well separated (top left in fig. 4). As thickness decreases the pulses merge and start to interfere. The resulting echo takes on the ringing appearance observed in the bottom left part of fig. 4 (similar to measured echoes in fig. 2). In the frequency domain power spectra (fig. 4 right) the separated pulses lead to a modulated curve of the single pulse frequency spectrum. The modulation contains a number of harmonics of a fundamental resonant interference frequency f_0 which comes from constructive interference of the successive reflections. This occur when $2\phi_2 = 2\pi m$, $m = 1, 2, \ldots$ for $r_{12} > 0$ and $r_{23} < 0$ which applies to solids immersed in water (a sign change in r_{12} or r_{23} would give an additional π phase shift). This condition leads to the simple relation $f_0 = 1/(2\tau_2) = v_2/(2d_2)$ or $\lambda_2 = 2d_2$. From this expression values of f_0 for SiC using sound velocity values from [9] were calculated and are shown in fig. 4 as red arrows which shows the ability for simple resonance prediction for multiple reflections..

It may be recognized that the terms in the numerator in eq. (2) corresponds to the first surface reflection and the first reflection from the back interface respectively, while the interference of the multiple subsequent internal reflections are represented by the term in the denominator. For interference to occur both r_{12} and r_{23} should be non-zero and the magnitude of the resonant dips depend on the magnitude of the reflection coefficients r_{12} and r_{23}.

For mild acoustic impedance mismatch the values will be small and vice-versa. In a power module, the exit medium can be either a solid material layer such as solder or a gas pocket (void) with additional multiple material layers beneath. While r_{12} for the first interface is fairly large at all sites due to the acoustic impedances mismatch between water and most solids, the r_{23} is only moderate at SiC and solder–copper interfaces while it attains a high value at void locations due to a big acoustic impedance mismatch between gas or liquid filled voids and solids. Thus distinct resonant dips should be more pronounced at void locations. As a consequence, by gating only the resonant frequency, locations with voids are highlighted but now with feature selectivity even in the case of strongly interfering and overlapping echoes.

So far the analysis has been limited to single layer resonances. Most power electronic structures such as power modules often contain multiple layers such as die, die attach, dbc sandwich structure, baseplate
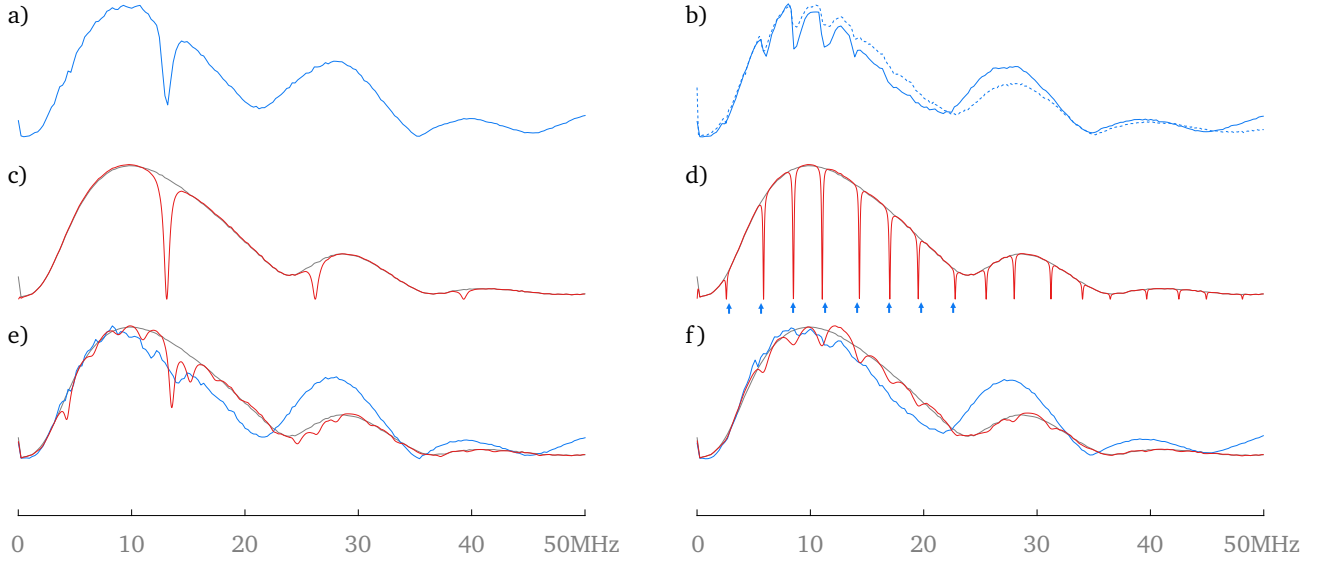
Figure 5: Comparison of experimental frequency spectra obtained form the presenteed models. Experimental frequency power spectra (blue full lines) were obtained at (a) SiC die void locations, (b) DBC -baseplate void locations, (e) SiC die intact solder, and (f) AlN DBC-baseplate intact solderlayer. In (b) the spectrum measured on a bare AlN DBC sample immersed in water is also shown for comparison (blue dashed line). Simulations (red lines) obtained from a reference waveform (grey lines) are shown for (b) single SiC slab in water, (d) AlN DBC sandwich structure in water, (e) complete soldered stack consisting of SiC die, 40 μm solder, AlN DBC, and 200 μm baseplate-solder layer on an AlSiC substrate, and (f) same as in (e) without the top die and die attach layer. Blue arrows in (d) show predicted f_{eff} values.

solder and baseplate so the extension of the analysis to multiple layered structures is of interest. Although the approach of summing the individual multiple reflections offered insight into the origin of the resonances it is a prohibitively complex approach for multilayer structures. A useful alternative method applicable in optics [10] as well is in acoustics [8] is based on matrix-representation and multiplication. The adaption of the method to the terminology of the present work is presented in the appendix.

6. Results and discussion

In order to compare the theoretical predictions with the experimental waveforms simulated power spectra $|S(f)|^2$ were obtained by combining calculated values of $r_{\text{eff}}(f)$, computed using the result in eq. (2) and the matrix method in the appendix, with a reference frequency power spectrum $A(f)$ (grey lines in fig. 5) obtained from scans on a polished copper block. For the simulations the acoustical properties listed in table 1 were used. Data for the solder alloy SAC 305 was used in simulations including solder layers.

In fig. 5 experimental FFT frequency power spectra (blue lines), obtained at four distinctly different locations, are compared to the theoretical predictions (red lines). For each location type the shown experimental waveforms were obtained by averaging spectra obtained at similar sites to reduce noise and improve the representation of the average properties of the surfaces.

In fig. 5a the experimental frequency spectrum obtained at die voids on the power module (like location ❷ in fig. 1) shows a single resonant dip. For comparison the simulated $|S(f)|^2$ using eq. (2) for an 0.5 mm SiC slab immersed in water is shown in fig. 5c. The simulation predicts a resonance frequency which is in close quantitative agreement with the experiment as well as two higher harmonics not observed experimentally. The corresponding simulation using the matrix method is not shown since this is identical with eq. (2) for single interfering layers.

In fig. 5b the experimental frequency spectrum for DBC void locations (e.g. ❶ or ❷) as well as the power spectrum obtained from SAM data for a single AlN DBC piece are shown (blue dashed line). The

6

Table 1: Table of acoustic properties used for simulation and mode predictions; *measured in this work; †rolled

Material	v [m/s]	ρ [10^3kg/m^3]	z [10^6Ns/m^3]
SiC	13100	3.211 [9]	42.1
SAC305	3380*	7.35*	24.8*
Sn†	3320	7.26 [11]	24.1
Cu†	5010	8.96 [11]	44.9
AlN	10287 [12]	3.26 [11]	34.46
AlSiC	8790*	3.0	26.4*

two curves are very similar supporting the notion that at the DBC voids the distinct dips in the spectra arise from the distinct DBC resonances. The simulated $|S(f)|^2$ of a single AlN DBC immersed in water is shown in fig. 5d and it can be seen that the predicted resonances are in good agreement with fig. 5b. From detailed measurements of dimensions of the single AlN DBC as well as bare AlN pieces it was found by comparison with the measurements that acoustic values for annealed copper from ref. [11] are unable to match the experiments while values of rolled copper lead to the agreement shown.

Since contrast is obtained between regions of voids and regions of intact solder layers, the FFT spectra of intact solder regions are also of interest. The experimental FFT power spectrum of intact SiC die solder locations and intact DBC solder locations are shown in fig. 5e and 5f (blue lines) respectively. Also shown are the corresponding simulated $|S(f)|^2$ spectra for a six layer soldered die–DBC–baseplate stack (fig. 5e) and for a similar stack but without die and die attach layer (fig. 5f).

Although these multilayer structures give a much more complicated mode pattern in the $|S(f)|^2$ spectra a qualitative agreement with the experimental data is observed in both fig. 5e and 5f in terms of number of modes and their relative strengths for frequencies below 15–20 MHz. The increased complexity with increasing number of layers is to be expected since more reflecting boundaries and layers potentially add more resonance conditions. Considering that the DBC structure in itself is a three layer system, the simulated curve in fig. 5d appears remarkably simple, almost resembling that of single layer structure. Such a phenomena could occur if the internal reflections between the ceramic and the copper layer were very weak. In that case the effective resonant mode of the combined layer thickness may be estimated using $f_{\text{eff}} = 1/(2\,\tau_{\text{eff}})$ where τ_{eff} is the effective transit time accross all three layers given by $\tau_{\text{eff}} = \tau_{\text{AlN}} + 2\,\tau_{\text{Cu}}$, and τ_{Cu} and τ_{AlN} are the transit times of the copper and AlN layers, respectively. From table 1 it can be seen that the acoustic impedance mismatch between Cu and AlN is only minor, but some internal reflections may exist. However to test the effective layer hypothesis, values of f_{eff} and corresponding higher harmonics were calculated and are included in fig. 5d as blue arrows. A fairly good agreement can be seen between the simple rule of thumb and the multilayer method, apart from a few of the resonances were the simple mode prediction is not exact due to the influence of inner layer reflections. Nevertheless the simpler approach provides a fast rule of thumb for estimating resonance positions for first level resonance assignment in experimental spectra.

As an overall observation the experimental spectra show less pronounced resonant features than the simulated ones. Moreover, the resonant dips are stronger at low frequency while at high frequency resonant dips are absent. The frequency dependence of the dip strength is likely due to increased attenuation (absorption) at higher frequencies and due to surface scattering effects, neither of which were included in the model due to lack of quantitative data. If the reflecting interface has significant roughness the assumptions of the derived models are somewhat challenged. Substantial parts of the soundwaves may undergo surface scattering at the interfaces and surfaces of the structure which leads to a wave randomization (in line with the effect in optics [13]). The effect will be that less sound will take part in the interference phenomena and in the case of complete randomization no resonances will be seen. This will be more pronounced at higher frequencies where the acoustic wavelength may become comparable with the size of the scattering in qualitative analogue with optical scattering [14]. Since DBC substrates can have a fairly rough surface this may be one plausible explanation of the high frequency behaviour. Obviously the lack of higher frequency modes limits the frequency span where analysis and selectivity based on such modes can be utilized. Despite the absence of modes at higher frequencies in the experimental spectra several modes may still be clearly

observed such as in the case of the DBC void spectrum in fig. 5b.

If several modes are available that allows the desired selectivity then the higher frequency one will show better resolution since the resolution limiting wavelength is inversely proportional to frequency. Thus the FD approach also allows selectivity of the wavelength used for image formation. An example of this is shown in fig. 6 where DBC–baseplate void selectivity contrast was targeted using resonances of different frequencies. From the powerspectrum seen in fig. 5b several dips were observed. FD images were formed by targeting three different modes and the result is shown in fig. 6a–c with corresponding frequency spans used shown in fig. 6d–f respectively.

As may be observed, the images formed with lower frequency are more blurry. The image formed with highest frequency also seems to form contrast at the die void locations albeit the contrast is inverted. By comparing with fig. 5a it can be seen that the selected frequency subspan is in the proximity of the mode of the SiC voids and hence for this specific higher morder mode the feature selectivity is slightly compromised but with the benefit of increased resolution. The availability of several modes thus offers several degrees of freedom to first identify the main features with feature selectivity and subsequent possibility for local resolution improvement.
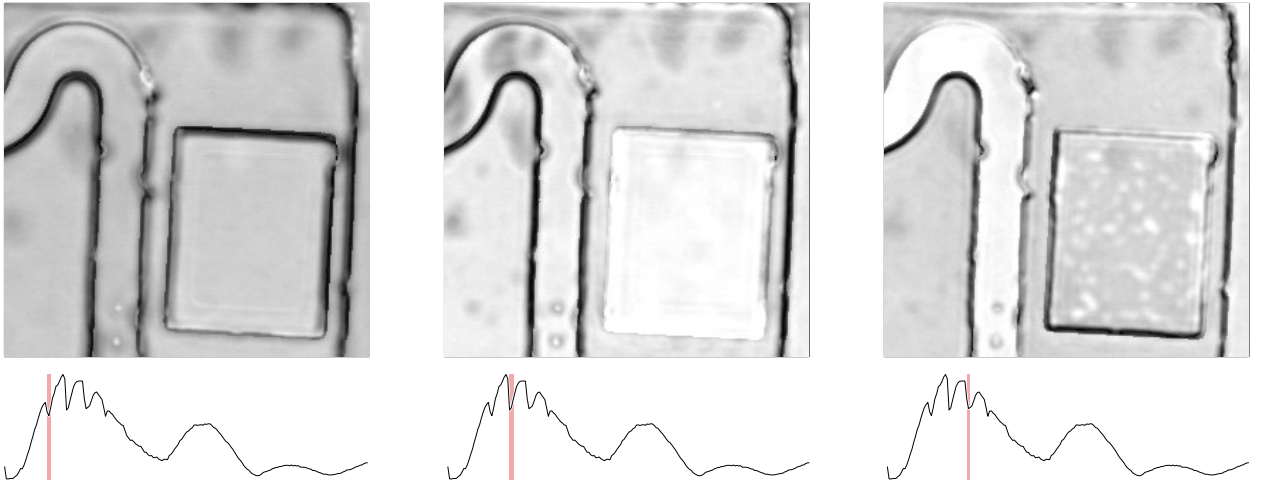

Figure 6: Influence of the frequency on the selected mode on the image resolution.

The fact that the resonance frequencies are linked to the thickness also implies that the frequency analysis provides a means of measuring thickness. The accuracy with which this can be done depends on how accurately the resonant dips can be assigned and the value of the frequency used. For high contrast reflections on either side as for the SiC chip with voids the quality factor of the dips is strong and accuracy seems mainly limited by the minimum frequency steps in the FFT, which are determined by the length of the time span used for the FFT transform. Although in theory a very large time span would yield ideal frequency resolution, for practical purposes only finite time span can be used partly because adding longer time spans may also add more noise and partly because unwanted secondary reflection echos may also be sampled which may complicate analysis.

For the FFT spectra in fig. 5a a frequency step of 250 kHz was obtained and the dip is measured at $f \approx 13$ MHz with an uncertainty of 2–4%. Using a longitudinal sound velocity of 13100 m/s [9] for SiC this corresponds to thickness of the die of $t = 0.5 \pm 0.02$ mm and a roundtrip time of flight $t_{\text{tof}} = 77 \pm 3$ ns. For a comparable time domain time-of-flight (TOF) method one could hope to obtain a time resolution $\delta t_{\text{res}} = 0.1 \Delta t_{\text{pulse}} \approx 20$ ns where $\Delta t_{\text{pulse}} \approx 200$ ns is the pulse width of the used transducer [15]. Thus for the current example the FD based thickness estimation provides an order of magnitude improvement estimation accuracy, not even considering the challenges of overlapping echoes in the time domain.

For acoustically thick samples ($\lambda \ll d$) the relative time domain TOF resolution will improve. This also implies a reduction of the f_0 frequency which worsens the relative accuracy of the FD approach if only

the fundamental mode is used. However in that case higher order modes may be selected as in fig. 6 and thickness estimation accuracy may be maintained. For acoustically very thin layers ($\lambda \gg d$) the single layer resonances will be out of the detectable range and a higher frequency transducer may be required, unless the thin layers couple with thicker layers (such as e.g. 40 μm solder on a DBC substrate). In the latter case under favourable conditions the impact of the thin layer may be observed as a shift of mode well within the detectable region and the predictions may still be tested.

As an alternative to thickness estimation, measured resonance frequencies can be used to measure material properties such as the speed of sound provided the thickness of the layer is known from supplementary measurements.

As an example, the FD approach was used on a sheet of uncoated SAC305 preform to measure the longitudinal sound velocity of the alloy. SAC305 is a Sn based alloy containing 3% Ag and 0.5% Cu. The question arose what influence the additional metal constituents might have on the acoustic properties, which would be needed for the estimation of solder thickness as commented above. From the frequency spectrum the fundamental frequency as well as three higher harmonics were observed and linear regression was used to establish the fundamental value $f_0 = 3.3$ MHz. Combined with a confirmation of the preform thickness of 0.008" = 0.205 mm this leads to a $v_L = 3380$ m/s in very close agreement with the value $v_L = 3320$ m/s of pure rolled Sn [11] as listed in table 1. The acoustic impedance was obtained from a measured density of the SAC305 preform sheet and the values are included in table 1.

Similarly the acoustic properties of the AlSiC baseplates are also of interest since AlSiC is a compound material not commonly listed in material tables. An AlSiC baseplate of thickness 3 mm was scanned and analysed using the FD approach. Several distinct dips were observed and from linear regression a fundamental resonance of $f_0 = 1.46$ MHz was derived, from which an acoustic velocity of $v_L = 8790$ m/s was obtained. Combined with the density informed from the supplier ($3.0 \cdot 10^3$ kg/m^3) the acoustic impedance $z_{AlSiC} = 26.4 \cdot 10^6$ Ns/m^3 was estimated in very good agreement with values of 26.35–$26.8 \cdot 10^6$ Ns/m^3 reported in ref. [16] although molding methods and grain size might not be comparable. The derived values are listed in table 1 and were used for the simulations in fig. 5e–f.

It is noted that the thickness estimation and material parameter measurements relies on the applicability of the formulas for the fundamental modes in the present analysis, which as stated applies to normal incidence conditions. For incident sound waves with $\theta \neq 0$ the angular dependence of the reflection and transmission coefficients as well shear wave, surface acoustic waves as well other more exotic modes may come into play[8]. The inclusion of the angular variation in the analysis of planar interface multi-layer structures is possible but substantially more complex in terms of interpretation. A key effect is that due to the inclination angle the phase term at a given angle θ is modified to $\phi = 2\pi f d \cos(\theta)$ [8]. For a signal that averages a span of angles the effective distance of the resonances will be some weighted average of $d \cos(\theta)$ and hence thickness may be estimated shorter than for normal incidence. However for the mildly focused transducer used here this has minor effects, as shown by the comparative quantitative analysis above, and adds little but complexity.

7. Conclusions

The frequency domain, when combined with physics-based interpretation guidelines, is a method that can be used by SAM operators to obtain increased layer selectivity and structure parameter extraction for analysis of multilayered power electronic structures.

The link between time domain and frequency domain analysis revealed the origin of the observed resonances. A quantitative comparison between experiments and model predictions for relevant power module configurations were presented together with a compilation of relevant acoustic data needed for calculations. The combined analysis clarifies the demonstrated physics-based feature selective contrast potential in power modules and gives rules of thumb for mode estimation and interpretation.

Appendix

For multilayered structures the combined reflection and transmission properties can be obtained by a matrix based method following that given in textbooks on optics such as [10] as well as acoustics [8]. The

adaptation to the terminology in this work is presented here. As above the analysis here will be limited to normal incidence. The sample system under consideration is depicted in fig. 7 and consists of n layers with specific sound velocity and density.
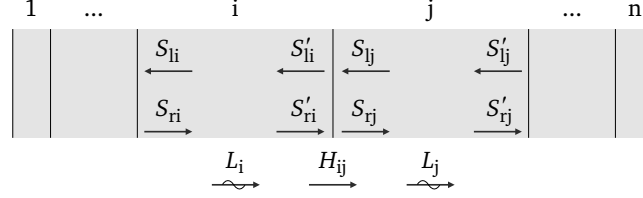

Figure 7: Schematic of the sound wave representation using left going (l) and right going (r) waves in a multi-layer stack. $\vec{S}_i = (S_{li}, S_{ri})$ represents the sound wave representation at the left side of the i'th layer and $\vec{S}'_i = (S'_{li}, S'_{ri})$ that at the right side.

The combined sound fields in each layer are represented as a sum of leftgoing and rightgoing waves. It can be shown that the sound fields $\vec{S}'_i$ and $\vec{S}_j$ at the boundary between layer i and j are related via

$$\vec{S}'_i = \frac{1}{\tau_{ij}} \left[\begin{array}{cc} 1 & r_{ij} \\ r_{ij} & 1 \end{array} \right] \vec{S}_j = H_{ij} \vec{S}_j$$

where H_{ij} denotes the transition matrix covering the effect of coupling across the i–j boundary. To account for the wavepropagation across each layer a phase propagator matrix is defined as

$$\vec{S}_i = \left[\begin{array}{cc} e^{i\phi_i} & 0 \\ 0 & e^{-i\phi_i} \end{array} \right] \vec{S}'_i = L_i \vec{S}'_i.$$

where ϕ_i is the phase term defined in eq. (3) for the i'th layer. The combined interference coupling between all layers are obtained by matrix multiplication of the propagation and transition matrices:

$$\vec{S}'_{\text{transducer}} H_{12} L_2 H_{23} L_3 H_{34} \ldots \vec{S}_{\text{exit}} = \left[\begin{array}{cc} M_{11} & M_{12} \\ M_{21} & M_{22} \end{array} \right] \vec{S}_{\text{exit}}.$$

The sound field on the transducer side $\vec{S}'_{\text{transducer}}$ consist of the right going incident S_i wave pulse and the left going reflected signal S_r, while the exit sound field $\vec{S}_{\text{exit}}$ only contain a right going transmitted signal S_t. With this information the effective reflection coefficient r_{eff} for the multi-layer stack can be identified as

$$r_{\text{eff}} = \frac{S_r}{S_i} = \frac{M_{12}}{M_{22}}.$$

The approach can be applied to an arbitrary number of layers, but algebraic solutions become extensive for even a few layers and numerical calculations are more convenient.

References

[1] U. Choi, F. Blaabjerg, S. Jørgensen, F. Iannuzzo, H. Wang, C. Uhrenfeldt, S. Munk-Nielsen, Power cycling test and failure analysis of molded Intelligent Power IGBT Module under different temperature swing durations, Microelectron. Reliab. 64. doi:10.1016/j.microrel.2016.07.020.

[2] S. Brand, F. Naumann, S. Tismer, B. Boettge, J. Rudzki, F. Osterwald, M. Petzold, Non-destructive assessment of reliability and quality related properties of power electronic devices for the in-line application of scanning acoustic microscopy, in: CIPS 2016; 9th International Conference on Integrated Power Electronics Systems, 2016, pp. 1–6.

[3] R. S. Gilmore, Industrial ultrasonic imaging and microscopy, J. Phys. D. Appl. Phys. 29 (6) (1999) 1389–1417. `doi:10.1088/0022-3727/29/6/001`.

[4] J. E. Semmens, L. W. Kessler, Application of Acoustic frequency domain imaging for the evaluation of advanced micro electronic packages, Microelectron. Reliab. 42.

[5] J. E. Semmens, L. W. Kessler, Acoustic micro imaging in the Fourier domain for evaluation of advanced packaging, J. Surface Mount Technology 16.

[6] S. Canumalla, L. W. Kessler, S. K. Bhattacharya, Characterization of thin layers in microelectronic packaging using acoustic microscopy, in: 4th International Conference on Adhesive Joining and Coating Technology in Electronics Manufacturing. Proceedings. Presented at Adhesives in Electronics 2000 (Cat. No.00EX431), 2000, pp. 225–231. `doi:10.1109/ADHES.2000.860606`.

[7] S. Canumalla, Thin layer acoustic image interpretation and metrology for microelectronics using a broadband model, IEEE Trans. Components Packag. Technol. 28 (2) (2005) 353–365. `doi:10.1109/TCAPT.2005.848496`.

[8] T. Kundu (Ed.), Ultrasonic and Electromagnetic NDE for Structure and Material Characterization, CRC, 2012.

[9] Sic mechanical properties, elastic constants, lattice vibrations, Online, May 2018.
URL `http://www.ioffe.ru/SVA/NSM/Semicond/SiC/mechanic.html`

[10] T. E. F. Miles V. Klein, Optics, 2nd Edition, John Wiley & Sons, Inc., 1986.

[11] D. R. Lide (Ed.), Handbook of Chemistry and Physics, 84th Edition, CRC PRESS, 2003/2004.

[12] C. Caliendo, Analytical study of the propagation of fast longitudinal modes along wz-bn/aln thin acoustic waveguides, Sensors 15 (2) (2015) 2525–2537. `doi:10.3390/s150202525`.
URL `http://www.mdpi.com/1424-8220/15/2/2525`

[13] E. Yablonovitch, Statistical ray optics, J. Opt. Soc. Am. 72 (7) (1982) 899–907. `doi:10.1364/JOSA.72.000899`.
URL `http://www.osapublishing.org/abstract.cfm?URI=josa-72-7-899`

[14] D. R. H. C. F.Bohren, Absorption and Scattering of Light by Small Particles, Wiley Interscience, 1983.

[15] M. de Podesta, G. Sutton, R. Underwood, S. Legg, A. Steinitz, Practical acoustic thermometry with acoustic waveguides, International Journal of Thermophysics 31 (8) (2010) 1554–1566. `doi:10.1007/s10765-010-0793-x`.
URL `https://doi.org/10.1007/s10765-010-0793-x`

[16] O. Kuwahara, N. Wang, S. Ueha, Reconstruction of acoustic impedance distribution of functionally gradient materials by using reflection impulse response, Japanese Journal of Applied Physics 31 (S1) (1992) 102.
URL `http://stacks.iop.org/1347-4065/31/i=S1/a=102`